# Direction-of-Arrival Estimation for Noncircular Sources via Structured Least Squares–Based ESPRIT Using Three-Axis Crossed Array

**YUNMEI SHI**
**LEI HUANG,** Senior Member, IEEE
**CHENG QIAN,** Student Member, IEEE
Harbin Institute of Technology Shenzhen Graduate School
Shenzhen, China

**H. C. SO,** Fellow, IEEE
City University of Hong Kong
Hong Kong, China

**A structured least squares (SLS)–based ESPRIT algorithm for direction-of-arrival (DOA) estimation of strictly second-order noncircular signals using a crossed array is devised in this paper. Unlike the conventional ESPRIT for noncircular signals, which employs the least squares or total least squares, the proposed solution is able to exploit the overlapping structure of the subarray configurations to efficiently solve the shift-invariant equations (SIEs), ending up with the SLS solution for a three-axis crossed array. Moreover, an additional constraint requiring the SIEs of the three linear subarrays directed along the *x*-, *y*-, and *z*-axes to share the same set of eigenvectors is applied to solve the rank-deficiency problem. Consequently, the proposed approach provides more accurate DOA estimates, and its superiority over existing ESPRIT schemes is demonstrated via computer simulations.**

Manuscript received January 1, 2014; revised July 18, 2014, October 22, 2014; released for publication November 24, 2014.

DOI. No. 10.1109/TAES.2015.140003.

Refereeing of this contribution was handled by W. Blanding.

The work described in this paper was supported by the National Natural Science Foundation of China under Grants 61222106 and 61171187, and by the Shenzhen Kongqie talent program under Grant KQC201109020061A.

Authors' addresses: L. Huang, Shenzhen University, Information Engineering College, Shenzhen 518060, China, E-mail: (dr.lei.huang@ieee.org); Y. Shi, C. Qian, Harbin Institute of Technology Shenzhen Graduate School, Shenzhen 518055, China; H. C. So, City University of Hong Kong, Electronic Engineering Department, Tat Chee Avenue, Kowloon, Hong Kong, 852, China.



## I. INTRODUCTION

Direction finding of signals impinging on an array is an important research topic in a variety of areas such as radar, sonar, mobile communications, and biomedical imaging. Numerous approaches have been proposed for high-resolution direction-of-arrival (DOA) estimation, including extrema-searching [1], polynomial-rooting [2], and matrix-shifting [3] techniques. In this paper, we consider the third category, that is, the estimation of signal parameters via rotational invariance techniques (ESPRIT)-like methods [4]. As a matrix-shifting approach, the ESPRIT algorithm is able to efficiently utilize the shift-invariant structure of the signal subspace and provides closed-form solution for DOA estimation. Consequently, it has received considerable attention. The ESPRIT-like algorithms are usually solved via least squares (LS) or total least squares (TLS), which turns out to be suboptimal due to the overlapping subarray configurations. A method known as structured total least norm (STLN) has been proposed for computing the solution to an overdetermined linear system, i.e., $\boldsymbol{Ax} \approx \boldsymbol{b}$, with possible errors in both $\boldsymbol{A}$ and $\boldsymbol{b}$ [5, 6]. Thereby, the STLN preserves the affine structure of $\boldsymbol{A}$, such as Toeplitz or Hankel structure. However, the STLN is not applicable to ESPRIT-like algorithms because the shift-invariant equations (SIEs) do not have the affine structure [7]. Owing to the highly structured property of the SIE, a structured least squares (SLS) method [7], which uses the same approximation as the STLN, namely, a second-order term in the expansion of the residual matrix is neglected, is preferable over the LS or TLS if overlapping subarray configurations are involved.

The ESPRIT-like algorithm was originally proposed for the one-dimensional DOA estimation in azimuth only and restricted to the range of $[0, \pi]$ [8]. In order to resolve a larger range of angles, planar antenna structures have to be utilized, e.g., circular arrays [9], rectangular arrays, and crossed arrays [10]. Such structures allow not only the azimuth angle but also the elevation angle to be taken into account. The ESPRIT algorithm has been developed for a three-axis crossed array in [11, 12] for joint estimation of the azimuth and elevation angles. As the crossed array can provide a larger aperture, it offers better resolution for a given number of elements than other multidimensional uniform array geometries [11, 13].

To further enhance the performance of the DOA estimators, besides the spatial structure of the antennas, the temporal properties of the signals, such as the noncircular (NC) property, can also be employed. The NC signals, such as binary phase shift keying (BPSK), offset quadrature phase shift keying (QPSK), pulse-amplitude modulation (PAM), and amplitude shift keying (ASK) modulated signals, have been widely used in many modern communication systems. By using the NC properties of the received signals, a number of improved subspace-based DOA estimators have been proposed, such

as the NC-MUSIC [14], NC-root-MUSIC [15], NC-ESPRIT [16], and NC unitary ESPRIT [17, 18]. The NC ESPRIT-like algorithms can double the array aperture and reduce the estimation errors.

In this paper, by using the structure of the three-axis crossed array along with the NC properties of the arriving signals, we devise an SLS-based NC-ESPRIT (SLS-NC-ESPRIT) for DOA estimation. Owing to the highly structured property of the SIEs, the SLS method can provide more accurate DOA estimates. For the three-axis crossed array, the LS, TLS, and SLS methods will break down when two or more arriving signals have the same projection onto the $x$-, $y$-, or $z$-axis because they cannot solve the rank-deficiency problem. As a result, an additional constraint requiring the SIEs of the three linear subarrays directed along the $x$-, $y$-, and $z$-axes to share the same set of eigenvectors is included. Moreover, the proposed SLS-NC-ESPRIT can provide better performance than the SLS method for the three-axis crossed array in [12] because the former is able to efficiently exploit the NC properties of the signals, while the latter cannot.

The rest of the paper is organized as follows. In Section II, the data model is presented. In Section III, we review the ESPRIT and NC-ESPRIT algorithms with three-axis crossed array structure and devise the SLS-NC-ESPRIT solution. In Section IV, simulation results are provided for performance comparison. Finally, Section V draws the conclusion.

The following notations are used throughout the paper. Matrices and vectors are represented by bold uppercase and bold lowercase symbols, respectively. Superscripts $(\cdot)^T$, $(\cdot)^H$, $(\cdot)^*$, and $(\cdot)^\dagger$ stand for transpose, conjugate transpose, conjugate, and pseudo-inverse, respectively. The symbols $\boldsymbol{I}_M$, $\boldsymbol{0}_{M\times K}$ and $\boldsymbol{\Pi}_M$ denote the $M \times M$ identity matrix, $M \times K$ zero matrix, and $M \times M$ exchange matrix, respectively. The Kronecker product is represented by $\otimes$, and vec$\{\cdot\}$ denotes the vectorization operator that maps the $m \times n$ matrix into an $mn \times 1$ column vector. The symbols $E\{\cdot\}$ and $|\cdot|$ stand for mathematical expectation and absolute value, respectively.

## II. PROBLEM FORMULATION

Consider a three-axis crossed array as shown in Fig. 1. It consists of three linear subarrays directed along the $x$-, $y$-, and $z$-axes, with the origin being the common geometric center. Assume that all antenna elements are identical and isotropic, and that the interelement spacing $\delta$ is equal on all three axes. Consider the three-axis crossed array with $M$ antennas receiving narrowband signals from $d$ far-field sources. Here, $M = M_x + M_y + M_z$, where $M_x$, $M_y$, and $M_z$ are the numbers of elements in the $x$-, $y$-, and $z$-directed subarrays, respectively. The array measurements are modeled as

$$\boldsymbol{x}(t) = \boldsymbol{A}\boldsymbol{s}(t) + \boldsymbol{n}(t) \tag{1}$$

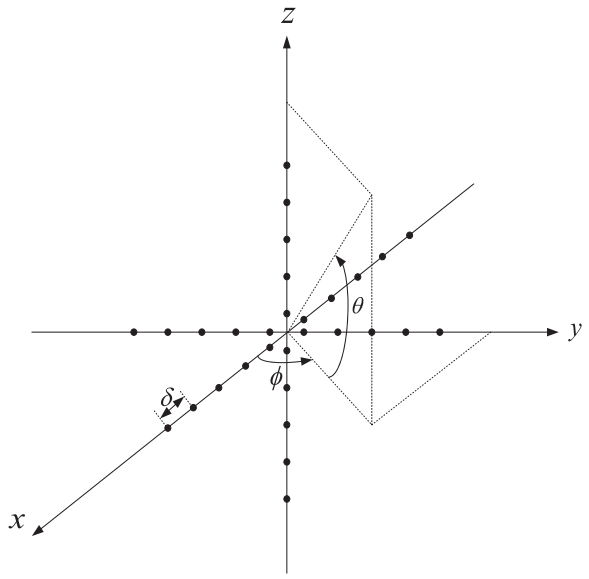


Fig. 1. Three-axis crossed array.

where $\boldsymbol{s}(t) = [\boldsymbol{s}_1(t), \cdots, \boldsymbol{s}_d(t)]^T$ is the signal vector, $\boldsymbol{n}(t) = [\boldsymbol{n}_1(t), \cdots, \boldsymbol{n}_M(t)]^T$ contains the additive sensor noise, and $\boldsymbol{A} = [\boldsymbol{a}(\theta_1, \phi_1), \cdots, \boldsymbol{a}(\theta_d, \phi_d)]$ is the steering matrix, which consists of $d$ array steering vectors $\boldsymbol{a}(\theta_i, \phi_i)$, $i = 1, \cdots, d$, with $\theta_i$ and $\phi_i$ representing the elevation and azimuth angles of the $i$th signal. Here, $d$ is known to the receiver or estimated by an information theoretic criterion, such as the Akaike information criterion (AIC) [20], minimum description length (MDL) [21], or their computationally efficient variants [22,23]. The array steering vector is given as

$$\boldsymbol{a}(\theta_i, \phi_i) = \begin{bmatrix} \boldsymbol{a}_x(\theta_i, \phi_i) \\ \boldsymbol{a}_y(\theta_i, \phi_i) \\ \boldsymbol{a}_z(\theta_i, \phi_i) \end{bmatrix}, i = 1, \ldots, d, \tag{2}$$

where

$$\boldsymbol{a}_x(\theta_i, \phi_i) = \left[e^{-j\frac{Mx-1}{2}\mu_{xi}}, e^{-j\frac{Mx-3}{2}\mu_{xi}}, \cdots, e^{j\frac{Mx-1}{2}\mu_{xi}}\right]^T, \tag{3}$$

$$\boldsymbol{a}_y(\theta_i, \phi_i) = \left[e^{-j\frac{My-1}{2}\mu_{yi}}, e^{-j\frac{My-3}{2}\mu_{yi}}, \cdots, e^{j\frac{My-1}{2}\mu_{yi}}\right]^T, \tag{4}$$

$$\boldsymbol{a}_z(\theta_i, \phi_i) = \left[e^{-j\frac{Mz-1}{2}\mu_{zi}}, e^{-j\frac{Mz-3}{2}\mu_{zi}}, \cdots, e^{j\frac{Mz-1}{2}\mu_{zi}}\right]^T. \tag{5}$$

Here,

$$\mu_{xi} = \frac{2\pi}{\lambda_0}\delta\cos(\phi_i)\sin(\theta_i), \tag{6}$$

$$\mu_{yi} = \frac{2\pi}{\lambda_0}\delta\sin(\phi_i)\sin(\theta_i), \tag{7}$$

$$\mu_{zi} = \frac{2\pi}{\lambda_0}\delta\cos(\theta_i), \tag{8}$$

with $\lambda_0$ denoting the wavelength. It is assumed that the noise $\boldsymbol{n}(t)$ is a white Gaussian process with mean zero and covariance $\sigma_n^2 \boldsymbol{I}_M$. Moreover, it is uncorrelated with the signal vector $\boldsymbol{s}(t)$.

Suppose that the signals are strictly NC. In other words, the complex symbol amplitudes of signals lie on a line in the I/Q diagram, which may correspond to BPSK, offset QPSK, and PAM [18]. Consequently, the source symbol snapshot vector can be decomposed as [17]

$$\boldsymbol{s}(t) = \boldsymbol{\Psi} \boldsymbol{s}_o(t), \tag{9}$$

where the diagonal matrix $\boldsymbol{\Psi} = \text{diag}\{e^{j\varphi_1}, \ldots, e^{j\varphi_d}\}$ contains the initial complex phase shift of each source, and $\boldsymbol{s}_o(t)$ is the real-valued data vector.

## III. PROPOSED ALGORITHM

### A. Motivation

We briefly review the ESPRIT and NC-ESPRIT algorithms [16] and extend them from the uniform linear array (ULA) to the three-axis crossed array case. We start by finding the ESPRIT solution for each of the linear subarrays. Based on the assumption above, the covariance matrix for the data vector $\boldsymbol{x}(t)$ can be written as

$$\boldsymbol{R}_x = E\left\{\boldsymbol{x}(t)\boldsymbol{x}^H(t)\right\} = \boldsymbol{A}\boldsymbol{R}_s\boldsymbol{A}^H + \sigma_n^2 \boldsymbol{I}_M, \tag{10}$$

where $\sigma_n^2$ is the noise power at each antenna, and

$$\boldsymbol{R}_s = E\left\{\boldsymbol{s}(t)\boldsymbol{s}^H(t)\right\}. \tag{11}$$

By using the spectral theorem, $\boldsymbol{R}_x$ can be decomposed as

$$\boldsymbol{R}_x = \boldsymbol{U}\boldsymbol{\Sigma}\boldsymbol{U}^H, \tag{12}$$

where $\boldsymbol{\Sigma} = \text{diag}\{\lambda_1, \ldots, \lambda_M\}$, with $\lambda_1 \geq \ldots \geq \lambda_d \geq \lambda_{d+1} = \ldots = \lambda_M = \sigma_n^2$ being the eigenvalues, and $\boldsymbol{U} = [\boldsymbol{u}_1, \ldots, \boldsymbol{u}_M]$, with $\boldsymbol{u}_i$, $i = 1, \ldots, M$, being the corresponding eigenvectors. It follows that $\boldsymbol{R}_x = \boldsymbol{U}_s\Sigma_s\boldsymbol{U}_s^H + \sigma_n^2\boldsymbol{U}_n\boldsymbol{U}_n^H$ with $\boldsymbol{\Sigma}_s = \text{diag}\{\lambda_1, \ldots, \lambda_d\}$, $U_s = [\boldsymbol{u}_1, \ldots, \boldsymbol{u}_d]$, and $\boldsymbol{U}_n = [\boldsymbol{u}_{d+1}, \ldots, \boldsymbol{u}_M]$. According to (10), we get

$$\boldsymbol{A}\boldsymbol{R}_s\boldsymbol{A}^H + \sigma_n^2\boldsymbol{I}_M = \boldsymbol{U}_s\boldsymbol{\Sigma}_s\boldsymbol{U}_s^H + \sigma_n^2\boldsymbol{U}_n\boldsymbol{U}_n^H. \tag{13}$$

With the use of $\boldsymbol{U}_s\boldsymbol{U}_s^H + \boldsymbol{U}_n\boldsymbol{U}_n^H = \boldsymbol{I}_M$ and (13), we obtain

$$\begin{aligned}\boldsymbol{U}_s &= \boldsymbol{A}\boldsymbol{R}_s\boldsymbol{A}^H\boldsymbol{U}_s\left[\boldsymbol{\Sigma}_s - \sigma_n^2\boldsymbol{I}_d\right]^{-1} \\ &\triangleq \boldsymbol{A}\boldsymbol{T},\end{aligned} \tag{14}$$

where $\boldsymbol{T} = \boldsymbol{R}_s\boldsymbol{A}^H\boldsymbol{U}_s[\boldsymbol{\Sigma}_s - \sigma_n^2\boldsymbol{I}_d]^{-1}$ is a nonsingular matrix. As a result, $\boldsymbol{U}_s$ is called the signal subspace. The relationship in (14) is utilized to derive the ESPRIT solution given below.

The selection matrices with maximum overlap of the subarrays for the ESPRIT are defined as

$$\boldsymbol{J}_{\xi 1} = [\boldsymbol{I}_{M_\xi - 1} \quad \boldsymbol{0}_{(M_\xi - 1)\times 1}], \tag{15}$$

$$\boldsymbol{J}_{\xi 2} = [\boldsymbol{0}_{(M_\xi - 1)\times 1} \quad \boldsymbol{I}_{M_\xi - 1}], \tag{16}$$

where $\xi \in \{x, y, z\}$. Thus, the selection matrices of the three-axis crossed array are given by

$$\boldsymbol{K}_{xl} = [\boldsymbol{J}_{xl} \quad \boldsymbol{0}_{(M_x-1)\times M_y} \quad \boldsymbol{0}_{(M_x-1)\times M_z}], l = 1, 2, \tag{17}$$

$$\boldsymbol{K}_{yl} = [\boldsymbol{0}_{(M_y-1)\times M_x} \quad \boldsymbol{J}_{yl} \quad \boldsymbol{0}_{(M_y-1)\times M_z}], l = 1, 2, \tag{18}$$

$$\boldsymbol{K}_{zl} = [\boldsymbol{0}_{(M_z-1)\times M_x} \quad \boldsymbol{0}_{(M_z-1)\times M_y} \quad \boldsymbol{J}_{zl}], l = 1, 2. \tag{19}$$

As each subarray is shift-invariant, we get

$$\boldsymbol{K}_{\xi 1}\boldsymbol{A}\boldsymbol{\Phi}_\xi = \boldsymbol{K}_{\xi 2}\boldsymbol{A}, \xi \in \{x, y, z\}, \tag{20}$$

Where $\boldsymbol{\Phi}_\xi = \text{diag}\{e^{ju_{\xi 1}}, \ldots, e^{ju_{\xi d}}\} \in \mathbb{C}^{d\times d}$. According to (14), we obtain

$$\boldsymbol{K}_{\xi 1}\boldsymbol{U}_s\boldsymbol{\Upsilon}_\xi = \boldsymbol{K}_{\xi 2}\boldsymbol{U}_s, \tag{21}$$

where

$$\boldsymbol{\Upsilon}_\xi = \boldsymbol{T}^{-1}\boldsymbol{\Phi}_\xi\boldsymbol{T}. \tag{22}$$

In order to take advantage of the benefits associated with the NC sources, we apply widely linear processing and define the augmented measurement data vector $\boldsymbol{x}^{(nc)}(t)$ according to [17, 18] as

$$\boldsymbol{x}^{(nc)}(t) = \begin{bmatrix} \boldsymbol{x}(t) \\ \boldsymbol{\Pi}_M\boldsymbol{x}^*(t) \end{bmatrix} \in \mathbb{C}^{2M}. \tag{23}$$

Note that the exchange matrix $\boldsymbol{\Pi}_M$ used in [17, 18] to facilitate the real-valued implementation of NC unitary ESPRIT is not a requirement for the NC-ESPRIT here. We define the augmented measurement matrix $\boldsymbol{x}^{(nc)}(t)$ as (23) to correspond with [17, 18]. Substituting (1) and (9) into (23) yields

$$\begin{aligned}\boldsymbol{x}^{(nc)}(t) &= \begin{bmatrix} \boldsymbol{A}\boldsymbol{s}(t) \\ \boldsymbol{\Pi}_M\boldsymbol{A}^*\boldsymbol{s}^*(t) \end{bmatrix} + \begin{bmatrix} \boldsymbol{n}(t) \\ \boldsymbol{\Pi}_M\boldsymbol{n}^*(t) \end{bmatrix} \\ &= \begin{bmatrix} \boldsymbol{A} \\ \boldsymbol{\Pi}_M\boldsymbol{A}^*\boldsymbol{\Psi}^*\boldsymbol{\Psi}^* \end{bmatrix}\boldsymbol{s}(t) + \begin{bmatrix} \boldsymbol{n}(t) \\ \boldsymbol{\Pi}_M\boldsymbol{n}^*(t) \end{bmatrix} \\ &\triangleq \boldsymbol{A}^{(nc)}\boldsymbol{s}(t) + \boldsymbol{n}^{(nc)}(t),\end{aligned} \tag{24}$$

$$\boldsymbol{K}_{x1}^{(nc)} = \begin{bmatrix} \boldsymbol{J}_{x1} & \boldsymbol{0}_{(M_x-1)\times M_y} & \boldsymbol{0}_{(M_x-1)\times M_z} & \boldsymbol{0}_{(M_x-1)\times M_z} & \boldsymbol{0}_{(M_x-1)\times M_y} & \boldsymbol{0}_{(M_x-1)\times M_x} \\ \boldsymbol{0}_{(M_x-1)\times M_x} & \boldsymbol{0}_{(M_x-1)\times M_y} & \boldsymbol{0}_{(M_x-1)\times M_z} & \boldsymbol{0}_{(M_x-1)\times M_z} & \boldsymbol{0}_{(M_x-1)\times M_y} & \boldsymbol{\Pi}_{M_x-1}\boldsymbol{J}_{x2}\boldsymbol{\Pi}_{M_x} \end{bmatrix}, \tag{25}$$

$$\boldsymbol{K}_{x2}^{(nc)} = \begin{bmatrix} \boldsymbol{J}_{x2} & \boldsymbol{0}_{(M_x-1)\times M_y} & \boldsymbol{0}_{(M_x-1)\times M_z} & \boldsymbol{0}_{(M_x-1)\times M_z} & \boldsymbol{0}_{(M_x-1)\times M_y} & \boldsymbol{0}_{(M_x-1)\times M_x} \\ \boldsymbol{0}_{(M_x-1)\times M_x} & \boldsymbol{0}_{(M_x-1)\times M_y} & \boldsymbol{0}_{(M_x-1)\times M_z} & \boldsymbol{0}_{(M_x-1)\times M_z} & \boldsymbol{0}_{(M_x-1)\times M_y} & \boldsymbol{\Pi}_{M_x-1}\boldsymbol{J}_{x1}\boldsymbol{\Pi}_{M_x} \end{bmatrix}, \tag{26}$$

$$\boldsymbol{K}_{y1}^{(nc)} = \begin{bmatrix} \boldsymbol{0}_{(M_y-1)\times M_x} & \boldsymbol{J}_{y1} & \boldsymbol{0}_{(M_y-1)\times M_z} & \boldsymbol{0}_{(M_y-1)\times M_z} & \boldsymbol{0}_{(M_y-1)\times M_y} & \boldsymbol{0}_{(M_y-1)\times M_x} \\ \boldsymbol{0}_{(M_y-1)\times M_x} & \boldsymbol{0}_{(M_y-1)\times M_y} & \boldsymbol{0}_{(M_y-1)\times M_z} & \boldsymbol{0}_{(M_y-1)\times M_z} & \boldsymbol{\Pi}_{M_y-1}\boldsymbol{J}_{y2}\boldsymbol{\Pi}_{M_y} & \boldsymbol{0}_{(M_y-1)\times M_z} \end{bmatrix}, \tag{27}$$

$$\boldsymbol{K}_{y2}^{(nc)} = \begin{bmatrix} \boldsymbol{0}_{(M_y-1)\times M_x} & \boldsymbol{J}_{y2} & \boldsymbol{0}_{(M_y-1)\times M_z} & \boldsymbol{0}_{(M_y-1)\times M_z} & \boldsymbol{0}_{(M_y-1)\times M_y} & \boldsymbol{0}_{(M_y-1)\times M_x} \\ \boldsymbol{0}_{(M_y-1)\times M_x} & \boldsymbol{0}_{(M_y-1)\times M_y} & \boldsymbol{0}_{(M_y-1)\times M_z} & \boldsymbol{0}_{(M_y-1)\times M_z} & \boldsymbol{\Pi}_{M_y-1}\boldsymbol{J}_{y1}\boldsymbol{\Pi}_{M_y} & \boldsymbol{0}_{(M_y-1)\times M_z} \end{bmatrix}, \tag{28}$$

$$\boldsymbol{K}_{z1}^{(nc)} = \begin{bmatrix} \boldsymbol{0}_{(M_z-1)\times M_x} & \boldsymbol{0}_{(M_z-1)\times M_y} & \boldsymbol{J}_{z1} & \boldsymbol{0}_{(M_z-1)\times M_z} & \boldsymbol{0}_{(M_z-1)\times M_y} & \boldsymbol{0}_{(M_z-1)\times M_x} \\ \boldsymbol{0}_{(M_z-1)\times M_x} & \boldsymbol{0}_{(M_z-1)\times M_y} & \boldsymbol{0}_{(M_z-1)\times M_z} & \boldsymbol{\Pi}_{M_z-1}\boldsymbol{J}_{z2}\boldsymbol{\Pi}_{M_z} & \boldsymbol{0}_{(M_z-1)\times M_y} & \boldsymbol{0}_{(M_z-1)\times M_x} \end{bmatrix}, \tag{29}$$

$$\boldsymbol{K}_{z2}^{(nc)} = \begin{bmatrix} \boldsymbol{0}_{(M_z-1)\times M_x} & \boldsymbol{0}_{(M_z-1)\times M_y} & \boldsymbol{J}_{z2} & \boldsymbol{0}_{(M_z-1)\times M_z} & \boldsymbol{0}_{(M_z-1)\times M_y} & \boldsymbol{0}_{(M_z-1)\times M_x} \\ \boldsymbol{0}_{(M_z-1)\times M_x} & \boldsymbol{0}_{(M_z-1)\times M_y} & \boldsymbol{0}_{(M_z-1)\times M_z} & \boldsymbol{\Pi}_{M_z-1}\boldsymbol{J}_{z1}\boldsymbol{\Pi}_{M_z} & \boldsymbol{0}_{(M_z-1)\times M_y} & \boldsymbol{0}_{(M_z-1)\times M_x} \end{bmatrix}, \tag{30}$$

where $\boldsymbol{A}^{(nc)}$ can be taken as the extended array steering matrix with a virtual doubling of the sensor elements, and $\boldsymbol{n}^{(nc)}(t)$ represents the extended noise vector. It should be noted that the virtual doubling sensor elements improve the estimation resolution and increase the number of detectable sources.

Let $\boldsymbol{X}^{(nc)}$ be a $2M \times N$ complex data matrix composed of $N$ snapshots $\boldsymbol{x}^{nc}(t_n)$, where $1 \le n \le N$. A number of NC ESPRIT–like algorithms for ULA have been devised [16–18]. However, exploiting the NC properties of the signals for the three-axis crossed array has not yet been studied in the literature. Based on the ESPRIT for a three-axis crossed array [12], we extend the selection matrices of the three-axis crossed array in (17) to (19) to the NC cases, which are shown at the bottom of next page. Note that the structure of the selection matrices is related to the definition of the augmented sample matrix $\boldsymbol{X}^{(nc)}$.

As each subarray of the three-axis crossed array is shift-invariant, according to [19], $\boldsymbol{A}^{(nc)}$ also possesses the shift invariance property

$$\boldsymbol{K}_{\xi 1}^{(nc)}\boldsymbol{A}^{(nc)}\boldsymbol{\Phi}_{\xi} = \boldsymbol{K}_{\xi 2}^{(nc)}\boldsymbol{A}^{(nc)}, \tag{31}$$

where $\xi \in \{x, y, z\}$.

Based on the data model in (23), we get the estimate of the signal subspace, i.e., $\hat{\boldsymbol{U}}_s^{(nc)}$, by computing the $d$ left singular vectors of $\boldsymbol{X}^{(nc)}$ associated with the $d$ dominant singular values. The $\boldsymbol{A}^{(nc)}$ and $\hat{\boldsymbol{U}}_s^{(nc)}$ span approximately the same column space, namely, $\hat{\boldsymbol{U}}_s^{(nc)} \approx \boldsymbol{A}^{(nc)}\boldsymbol{T}^{(nc)}$, where $\boldsymbol{T}^{(nc)} \in \mathbb{C}^{d\times d}$ is a nonsingular matrix. Similar to the ESPRIT, the SIEs in (21) for NC signals can be expressed as

$$\boldsymbol{K}_{\xi 1}^{(nc)}\hat{\boldsymbol{U}}_s^{(nc)}\boldsymbol{\Upsilon}_{\xi} = \boldsymbol{K}_{\xi 2}^{(nc)}\hat{\boldsymbol{U}}_s^{(nc)}, \quad \xi \in \{x, y, z\}. \tag{32}$$

The conventional approach to solve (32) is based on LS, i.e., $\boldsymbol{\Upsilon}_{\xi}^{\mathrm{LS}} = (\boldsymbol{K}_{\xi 1}^{(nc)}\hat{\boldsymbol{U}}_s^{(nc)})^{\dagger}(\boldsymbol{K}_{\xi 2}^{(nc)}\hat{\boldsymbol{U}}_s^{(nc)})$. However, the LS method assumes that $\boldsymbol{K}_{\xi 1}^{(nc)}\hat{\boldsymbol{U}}_s^{(nc)}$ is known without error, whereas $\boldsymbol{K}_{\xi 2}^{(nc)}\hat{\boldsymbol{U}}_s^{(nc)}$ is subject to error, which is obviously not appropriate in practical applications. Unlike the LS solution, the TLS can minimize the perturbations $\Delta\hat{\boldsymbol{U}}_{s1}^{(nc)}$ and $\Delta\hat{\boldsymbol{U}}_{s2}^{(nc)}$ in $\boldsymbol{K}_{\xi 1}^{(nc)}\hat{\boldsymbol{U}}_s^{(nc)}$ and $\boldsymbol{K}_{\xi 2}^{(nc)}\hat{\boldsymbol{U}}_s^{(nc)}$, respectively. Consequently, it is more accurate than the LS. However, the TLS is appropriate only if the two subarrays do not share any element. Instead, the SLS method is more appropriate when the two subarrays of each linear array directed along the $x$-, $y$-, and $z$-axes have overlapping elements, since it considers the specific relationship between subarrays. This thereby motivates us to employ the SLS approach to solve the SIEs in (32) for the NC signals in the next subsection, leading to the considerably enhanced accuracy in joint estimation of elevation and azimuth.

## B. Derivation

In this subsection, we employ the SLS technique to solve (32). As $\hat{\boldsymbol{U}}_s^{(nc)}$ only spans the noise-corrupted signal subspace, assuming that there exists a small perturbation $\Delta\hat{\boldsymbol{U}}_s^{(nc)}$ in this signal subspace, an improved signal subspace estimate can be expressed as $\tilde{\boldsymbol{U}}_s^{(nc)} = \hat{\boldsymbol{U}}_s^{(nc)} + \Delta\hat{\boldsymbol{U}}_s^{(nc)}$. Let us define the residual matrix as

$$\boldsymbol{R}_\xi(\tilde{\boldsymbol{U}}_s^{(nc)}, \boldsymbol{\Upsilon}_\xi) = \boldsymbol{K}_{\xi 1}^{(nc)}\tilde{\boldsymbol{U}}_s^{(nc)}\boldsymbol{\Upsilon}_\xi - \boldsymbol{K}_{\xi 2}^{(nc)}\tilde{\boldsymbol{U}}_s^{(nc)}, \xi \in \{x, y, z\}. \tag{33}$$

The method therefore proceeds by minimizing the Frobenius norm of $\boldsymbol{R}_\xi(\tilde{\boldsymbol{U}}_s^{(nc)}, \boldsymbol{\Upsilon}_\xi)$. Moreover, the Frobenius norm of $\Delta\hat{\boldsymbol{U}}_s^{(nc)}$ should be kept as small as possible. As a result, the improved estimates can be obtained by solving the following minimization problem:

$$\min_{\Delta\hat{U}_s^{(nc)}, \boldsymbol{\Upsilon}_\xi} \left\| \begin{bmatrix} \boldsymbol{R}_\xi(\tilde{\boldsymbol{U}}_s^{(nc)}, \boldsymbol{\Upsilon}_\xi) \\ \kappa \cdot \Delta\hat{\boldsymbol{U}}_s^{(nc)} \end{bmatrix} \right\|_F, \xi \in \{x, y, z\}. \tag{34}$$

Here, $\kappa = \sqrt{(2(M-3))/(\alpha 2M)}$ is a tuning factor that makes the minimization of $\Delta\hat{\boldsymbol{U}}_s^{(nc)}$ be independent of the dimensions of $\boldsymbol{R}_\xi(\tilde{\boldsymbol{U}}_s^{(nc)}, \boldsymbol{\Upsilon}_\xi)$. From [7], we conclude that if the value of $\alpha$ is larger than 1, the entries of $\Delta\hat{\boldsymbol{U}}_s^{(nc)}$ should be larger than the entries of $\boldsymbol{R}_\xi(\tilde{\boldsymbol{U}}_s^{(nc)}, \boldsymbol{\Upsilon}_\xi)$ in each step of the iterative procedure. Actually, as has been pointed out in [7], the SLS algorithm is not sensitive to the choice of $\alpha$. Denote the $(i, j)$ entries of $\boldsymbol{R}_\xi(\tilde{\boldsymbol{U}}_s^{(nc)}, \boldsymbol{\Upsilon}_\xi)$ and $\Delta\hat{\boldsymbol{U}}_s^{(nc)}$ by $r_{ij}$ and $e_{ij}$, respectively. The problem in (34) can then be rewritten as

$$\min_{\Delta\hat{U}_s^{(nc)}, \boldsymbol{\Upsilon}_\xi} \sum_{j=1}^{d}\left(\frac{\alpha}{2(M-3)d}\sum_{i=1}^{2(M-3)}|r_{ij}|^2 + \frac{1}{2Md}\sum_{i=1}^{2M}|e_{ij}|^2\right). \tag{35}$$

As the subarrays of the three-axis crossed array are linear, the matrix $\boldsymbol{K}_{\xi l}^{(nc)}\hat{\boldsymbol{U}}_s^{(nc)}, \xi \in \{x, y, z\}, l = 1, 2$, may be rank deficient when two or more arriving signals have the same projection onto the $\xi$-axis. As a result, the LS, TLS, and SLS methods will provide incorrect results on the particular $\xi$-axis. However, there is only one set of solutions, since the resulting matrices $\boldsymbol{\Upsilon}_\xi, \xi \in \{x, y, z\}$ share the same set of eigenvectors [11, 24]. A necessary and sufficient condition for two matrices $\boldsymbol{A}$ and $\boldsymbol{B}$ to share the same set of eigenvectors is that $\boldsymbol{AB} = \boldsymbol{BA}$ [12]. Using this property, the SLS method can be improved by exploiting the relationship between the matrices $\boldsymbol{\Upsilon}_\xi, \xi \in \{x, y, z\}$. Thus, we have

$$\boldsymbol{F}_1 = \boldsymbol{\Upsilon}_x\boldsymbol{\Upsilon}_y - \boldsymbol{\Upsilon}_y\boldsymbol{\Upsilon}_x = \boldsymbol{0}_{d\times d}, \tag{36}$$

$$\boldsymbol{F}_2 = \boldsymbol{\Upsilon}_y\boldsymbol{\Upsilon}_z - \boldsymbol{\Upsilon}_z\boldsymbol{\Upsilon}_y = \boldsymbol{0}_{d\times d}, \tag{37}$$

$$\boldsymbol{F}_3 = \boldsymbol{\Upsilon}_z\boldsymbol{\Upsilon}_x - \boldsymbol{\Upsilon}_x\boldsymbol{\Upsilon}_z = \boldsymbol{0}_{d\times d}. \tag{38}$$

We can find that (36) to (38) force the matrices $\boldsymbol{\Upsilon}_\xi, \xi \in \{x, y, z\}$ to share the same set of eigenvectors, enabling us to circumvent the rank-deficiency problem. As a result, the estimation accuracy can be considerably improved.

Following the algorithm [7] that solves an equation like (34) in an iterative procedure, an improved SLS method for unitary ESPRIT is derived in [12]. Analogous to the ESPRIT algorithm for a three-axis crossed array [12], the SLS-NC-ESPRIT extends the signal model to the augmented sample matrix case and updates the cost function as well as the tuning factor for NC signals. Moreover, an additional constraint for the NC signals is employed to circumvent the rank-deficiency problem. As a result, the SLS-NC-ESPRIT can provide much more accurate elevation and azimuth estimates by jointly minimizing the Frobenius norms of $\boldsymbol{F}_1$, $\boldsymbol{F}_2$, and $\boldsymbol{F}_3$ and applying the improved SLS method to solve the SIEs of the three-axis crossed array.

Let the residual matrices $\boldsymbol{F}_1$, $\boldsymbol{F}_2$, and $\boldsymbol{F}_3$ at the $k$th iteration be

$$\boldsymbol{R}(\tilde{\boldsymbol{U}}_{sk}^{(nc)}, \boldsymbol{\Upsilon}_{\xi k}) = \boldsymbol{K}_{\xi 1}^{(nc)}\tilde{\boldsymbol{U}}_{sk}^{(nc)}\boldsymbol{\Upsilon}_\xi - \boldsymbol{K}_{\xi 2}^{(nc)}\tilde{\boldsymbol{U}}_{sk}^{(nc)}, \tag{39}$$

$$\boldsymbol{F}_{1k} = \boldsymbol{\Upsilon}_{xk}\boldsymbol{\Upsilon}_{yk} - \boldsymbol{\Upsilon}_{yk}\boldsymbol{\Upsilon}_{xk}, \tag{40}$$

$$\boldsymbol{F}_{2k} = \boldsymbol{\Upsilon}_{yk}\boldsymbol{\Upsilon}_{zk} - \boldsymbol{\Upsilon}_{zk}\boldsymbol{\Upsilon}_{yk}, \tag{41}$$

$$\boldsymbol{F}_{3k} = \boldsymbol{\Upsilon}_{zk}\boldsymbol{\Upsilon}_{xk} - \boldsymbol{\Upsilon}_{xk}\boldsymbol{\Upsilon}_{zk}, \tag{42}$$

where $\xi \in \{x, y, z\}$. So the residual matrices $\boldsymbol{F}_1$, $\boldsymbol{F}_2$, and $\boldsymbol{F}_3$ at the $(k+1)$th iteration can be written as

$$\begin{aligned}&\boldsymbol{R}\left(\tilde{\boldsymbol{U}}_{s(k+1)}^{(nc)}, \boldsymbol{\Upsilon}_{\xi(k+1)}\right)\\ &= \boldsymbol{R}\left(\tilde{\boldsymbol{U}}_{sk}^{(nc)} + \Delta\hat{\boldsymbol{U}}_{s,k}^{(nc)}, \boldsymbol{\Upsilon}_{\xi k} + \Delta\boldsymbol{\Upsilon}_{\xi k}\right) \approx \mathbf{R}\left(\tilde{\boldsymbol{U}}_{sk}^{(nc)}, \boldsymbol{\Upsilon}_{\xi k}\right)\\ &\quad + \boldsymbol{K}_{\xi 1}^{(nc)}\tilde{\boldsymbol{U}}_{sk}^{(nc)}\Delta\boldsymbol{\Upsilon}_{\xi k} + \boldsymbol{K}_{\xi 1}^{(nc)}\Delta\hat{\boldsymbol{U}}_{sk}^{(nc)}\boldsymbol{\Upsilon}_{\xi k} - \boldsymbol{K}_{\xi 2}^{(nc)}\Delta\hat{\boldsymbol{U}}_{s,k}^{(nc)},\end{aligned} \tag{43}$$

$$\begin{aligned}\boldsymbol{F}_{1(k+1)} &= (\boldsymbol{\Upsilon}_{xk} + \Delta\boldsymbol{\Upsilon}_{xk})(\boldsymbol{\Upsilon}_{yk} + \Delta\boldsymbol{\Upsilon}_{yk})\\ &\quad -(\boldsymbol{\Upsilon}_{yk} + \Delta\boldsymbol{\Upsilon}_{yk})(\boldsymbol{\Upsilon}_{xk} + \Delta\boldsymbol{\Upsilon}_{xk})\\ &\approx \boldsymbol{F}_{1k} + \boldsymbol{\Upsilon}_{xk}\Delta\boldsymbol{\Upsilon}_{yk} + \Delta\boldsymbol{\Upsilon}_{xk}\boldsymbol{\Upsilon}_{yk}\\ &\quad -\boldsymbol{\Upsilon}_{yk}\Delta\boldsymbol{\Upsilon}_{xk} - \Delta\boldsymbol{\Upsilon}_{yk}\boldsymbol{\Upsilon}_{xk},\end{aligned} \tag{44}$$

$$\begin{aligned}\boldsymbol{F}_{2(k+1)} &= (\boldsymbol{\Upsilon}_{yk} + \Delta\boldsymbol{\Upsilon}_{yk})(\boldsymbol{\Upsilon}_{zk} + \Delta\boldsymbol{\Upsilon}_{zk})\\ &\quad -(\boldsymbol{\Upsilon}_{zk} + \Delta\boldsymbol{\Upsilon}_{zk})(\boldsymbol{\Upsilon}_{yk} + \Delta\boldsymbol{\Upsilon}_{yk})\\ &\approx \boldsymbol{F}_{2k} + \boldsymbol{\Upsilon}_{yk}\Delta\boldsymbol{\Upsilon}_{zk} + \Delta\boldsymbol{\Upsilon}_{yk}\boldsymbol{\Upsilon}_{zk}\\ &\quad -\boldsymbol{\Upsilon}_{zk}\Delta\boldsymbol{\Upsilon}_{yk} - \Delta\boldsymbol{\Upsilon}_{zk}\boldsymbol{\Upsilon}_{yk},\end{aligned} \tag{45}$$

$$\begin{aligned}\boldsymbol{F}_{3(k+1)} &= (\boldsymbol{\Upsilon}_{zk} + \Delta\boldsymbol{\Upsilon}_{zk})(\boldsymbol{\Upsilon}_{xk} + \Delta\boldsymbol{\Upsilon}_{xk})\\ &\quad -(\boldsymbol{\Upsilon}_{xk} + \Delta\boldsymbol{\Upsilon}_{xk})(\boldsymbol{\Upsilon}_{zk} + \Delta\boldsymbol{\Upsilon}_{zk})\\ &\approx \boldsymbol{F}_{3k} + \boldsymbol{\Upsilon}_{zk}\Delta\boldsymbol{\Upsilon}_{xk} + \Delta\boldsymbol{\Upsilon}_{zk}\boldsymbol{\Upsilon}_{xk}\\ &\quad -\boldsymbol{\Upsilon}_{xk}\Delta\boldsymbol{\Upsilon}_{zk} - \Delta\boldsymbol{\Upsilon}_{xk}\boldsymbol{\Upsilon}_{zk}.\end{aligned} \tag{46}$$

Note that the last approximations in (43) to (46) are obtained by neglecting the second-order terms. Given the matrices $\boldsymbol{C}_1 \in \mathbb{C}^{c_1\times c_2}$, $\boldsymbol{C}_2 \in \mathbb{C}^{c_2\times c_3}$, and $\boldsymbol{C}_3 \in \mathbb{C}^{c_3\times c_4}$, we obtain

$$\mathrm{vec}\{\boldsymbol{C}_1\boldsymbol{C}_2\boldsymbol{C}_3\} = \left(\boldsymbol{C}_3^T \otimes \boldsymbol{C}_1\right)\mathrm{vec}\{\boldsymbol{C}_2\}. \tag{47}$$

Applying vectorization to (43) to (46), we get

$$\begin{aligned}
&\mathrm{vec}\left\{\boldsymbol{R}\left(\tilde{\boldsymbol{U}}_{s(k+1)}^{(nc)}, \boldsymbol{\Upsilon}_{\xi(k+1)}\right)\right\} \\
&\quad\approx \mathrm{vec}\left\{\boldsymbol{R}\left(\tilde{\boldsymbol{U}}_{sk}^{(nc)}, \boldsymbol{\Upsilon}_{\xi k}\right)\right\} \\
&\qquad+\left[\boldsymbol{I}_d \otimes \left(\boldsymbol{K}_{\xi 1}^{(nc)}\tilde{\boldsymbol{U}}_{sk}^{(nc)}\right)\right]\mathrm{vec}\left\{\Delta\boldsymbol{\Upsilon}_{\xi k}\right\} \\
&\qquad+\left[\boldsymbol{\Upsilon}_{\xi k}^{T}\otimes \boldsymbol{K}_{\xi 1}^{(nc)} - \boldsymbol{I}_d \otimes \boldsymbol{K}_{\xi 2}^{(nc)}\right]\mathrm{vec}\left\{\Delta\hat{\boldsymbol{U}}_{s,k}^{(nc)}\right\}, \quad (48)
\end{aligned}$$

$$\begin{aligned}
&\mathrm{vec}\left\{\boldsymbol{F}_{1(k+1)}\right\} \\
&\quad\approx \mathrm{vec}\left\{\boldsymbol{F}_{1k}\right\} + \left[\boldsymbol{\Upsilon}_{yk}^{T}\otimes\boldsymbol{I}_d - \boldsymbol{I}_d\otimes\boldsymbol{\Upsilon}_{yk}\right]\mathrm{vec}\left\{\Delta\boldsymbol{\Upsilon}_{xk}\right\} \\
&\qquad+\left[\boldsymbol{I}_d\otimes\boldsymbol{\Upsilon}_{xk} - \boldsymbol{\Upsilon}_{xk}\otimes\boldsymbol{I}_d\right]\mathrm{vec}\left\{\Delta\boldsymbol{\Upsilon}_{yk}\right\}, \quad (49)
\end{aligned}$$

$$\begin{aligned}
&\mathrm{vec}\left\{\boldsymbol{F}_{2(k+1)}\right\} \\
&\quad\approx \mathrm{vec}\left\{\boldsymbol{F}_{2k}\right\} + \left[\boldsymbol{\Upsilon}_{zk}^{T}\otimes\boldsymbol{I}_d - \boldsymbol{I}_d\otimes\boldsymbol{\Upsilon}_{zk}\right]\mathrm{vec}\left\{\Delta\boldsymbol{\Upsilon}_{yk}\right\} \\
&\qquad+\left[\boldsymbol{I}_d\otimes\boldsymbol{\Upsilon}_{yk} - \boldsymbol{\Upsilon}_{yk}\otimes\boldsymbol{I}_d\right]\mathrm{vec}\left\{\Delta\boldsymbol{\Upsilon}_{zk}\right\}, \quad (50)
\end{aligned}$$

$$\begin{aligned}
&\mathrm{vec}\left\{\boldsymbol{F}_{3(k+1)}\right\} \\
&\quad\approx \mathrm{vec}\left\{\boldsymbol{F}_{3k}\right\} + \left[\boldsymbol{\Upsilon}_{xk}^{T}\otimes\boldsymbol{I}_d - \boldsymbol{I}_d\otimes\boldsymbol{\Upsilon}_{xk}\right]\mathrm{vec}\left\{\Delta\boldsymbol{\Upsilon}_{zk}\right\} \\
&\qquad+\left[\boldsymbol{I}_d\otimes\boldsymbol{\Upsilon}_{zk} - \boldsymbol{\Upsilon}_{zk}\otimes\boldsymbol{I}_d\right]\mathrm{vec}\left\{\Delta\boldsymbol{\Upsilon}_{xk}\right\}. \quad (51)
\end{aligned}$$

Meanwhile, let $\Delta\tilde{\boldsymbol{U}}_{s,k}^{(nc)} \triangleq \sum_{i=1}^{k-1}\Delta\hat{\boldsymbol{U}}_{s,i}^{(nc)}$ be the signal subspace change compared with the initial estimate $\hat{\boldsymbol{U}}_{s}^{(nc)}$ at the $k$th iteration step. The improved $\tilde{\boldsymbol{U}}_{sk}^{(nc)}$ is represented as

$$\tilde{\boldsymbol{U}}_{sk}^{(nc)} = \hat{\boldsymbol{U}}_{s}^{(nc)} + \Delta\tilde{\boldsymbol{U}}_{s,k}^{(nc)}. \quad (52)$$

From (43) to (51), the SLS problem is formulated in (53),

$$\begin{aligned}
\left\{\hat{\boldsymbol{\Upsilon}}_x, \hat{\boldsymbol{\Upsilon}}_y, \hat{\boldsymbol{\Upsilon}}_z\right\} &= \arg\min_{\Delta\boldsymbol{\Upsilon}_{\xi k}, \Delta\hat{\boldsymbol{U}}_{s,k}^{(nc)}} \\
&\times\left\|\begin{bmatrix}\mathrm{vec}\left\{\boldsymbol{R}(\tilde{\boldsymbol{U}}_{sk}^{(nc)}+\Delta\hat{\boldsymbol{U}}_{s,k}^{(nc)}, \boldsymbol{\Upsilon}_{xk})\right\}\\ \mathrm{vec}\left\{\boldsymbol{R}(\tilde{\boldsymbol{U}}_{sk}^{(nc)}+\Delta\hat{\boldsymbol{U}}_{s,k}^{(nc)}, \boldsymbol{\Upsilon}_{yk})\right\}\\ \mathrm{vec}\left\{\boldsymbol{R}(\tilde{\boldsymbol{U}}_{sk}^{(nc)}+\Delta\hat{\boldsymbol{U}}_{s,k}^{(nc)}, \boldsymbol{\Upsilon}_{zk})\right\}\\ \mathrm{vec}\left\{\boldsymbol{F}_{1k}\right\}\\ \mathrm{vec}\left\{\boldsymbol{F}_{2k}\right\}\\ \mathrm{vec}\left\{\boldsymbol{F}_{3k}\right\}\\ \tilde{\kappa}\cdot\mathrm{vec}\left\{\Delta\tilde{\boldsymbol{U}}_{s,k}^{(nc)}\right\}\end{bmatrix} + \mathbf{H}_k\cdot\begin{bmatrix}\mathrm{vec}\left\{\Delta\boldsymbol{\Upsilon}_{xk}\right\}\\ \mathrm{vec}\left\{\Delta\boldsymbol{\Upsilon}_{yk}\right\}\\ \mathrm{vec}\left\{\Delta\boldsymbol{\Upsilon}_{zk}\right\}\\ \mathrm{vec}\left\{\Delta\hat{\boldsymbol{U}}_{s,k}^{(nc)}\right\}\end{bmatrix}\right\|_F \quad (53)
\end{aligned}$$

where

$$\tilde{\kappa} = \sqrt{\frac{2(M-3)+3d}{\alpha 2M}} \quad (54)$$

provides a normalization that makes the minimization of $\mathrm{vec}\{\Delta\hat{\boldsymbol{U}}_{s}^{(nc)}\}$ independent of the sizes of the other matrices. Here, $\mathbf{H}_k$ is defined as (55). Minimizing the cost function in (53), we obtain the optimal estimates of $\boldsymbol{\Upsilon}_x$, $\boldsymbol{\Upsilon}_y$, and $\boldsymbol{\Upsilon}_z$, i.e., $\hat{\boldsymbol{\Upsilon}}_x$, $\hat{\boldsymbol{\Upsilon}}_y$, and $\hat{\boldsymbol{\Upsilon}}_z$. As a result, the optimal estimates of spatial frequencies $\mu_{xi}$, $\mu_{yi}$, and $\mu_{zi}$, where $i = 1, \ldots, d$, i.e., $\hat{\mu}_{xi}$, $\hat{\mu}_{yi}$, and $\hat{\mu}_{zi}$, $i = 1, \ldots, d$, are calculated from $\hat{\boldsymbol{\Upsilon}}_x$, $\hat{\boldsymbol{\Upsilon}}_y$, and $\hat{\boldsymbol{\Upsilon}}_z$ with the aid of eigendecomposition.

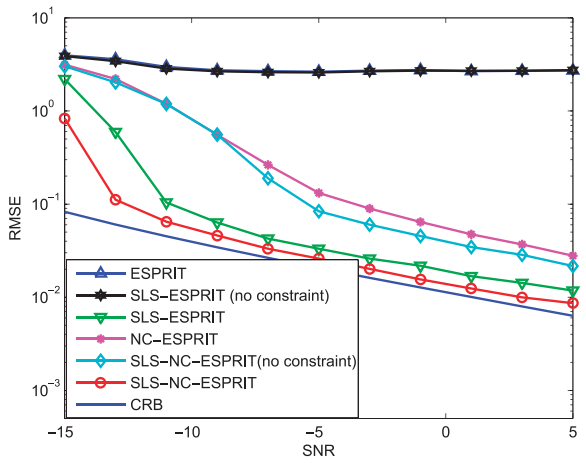


Fig. 2. RMSE of spatial frequency estimates versus SNR for $\theta_1 = \theta_2$, $\phi_1 \neq \phi_2$, $N = 300$.

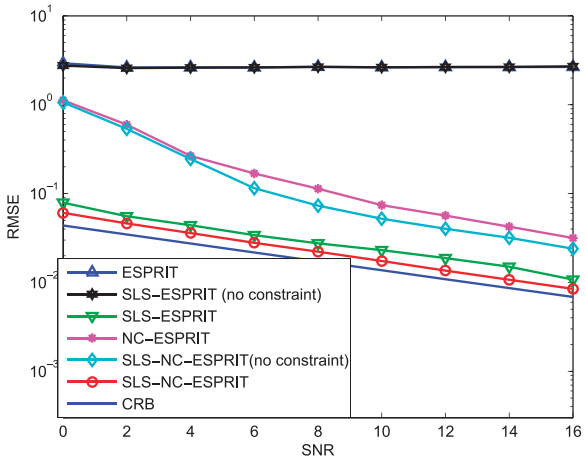


Fig. 3. RMSE of spatial frequency estimates versus SNR for $\theta_1 = \theta_2$, $\phi_1 \neq \phi_2$, $N = 20$.

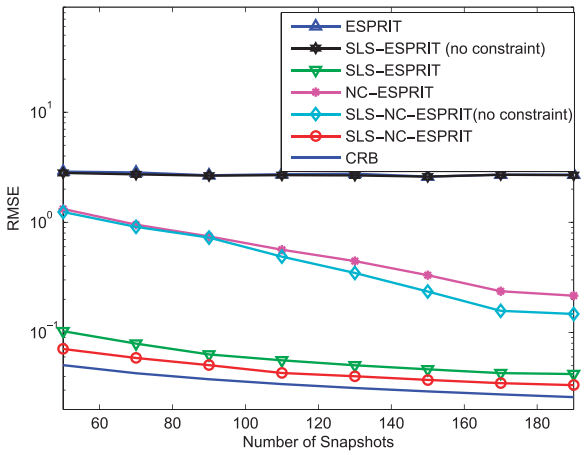


Fig. 4. RMSE of spatial frequency estimates versus snapshot number for $\theta_1 = \theta_2$, $\phi_1 \neq \phi_2$.

$$\mathbf{H}_k = \begin{bmatrix} I_d \otimes \left(\boldsymbol{K}_{x1}^{(nc)} \tilde{\boldsymbol{U}}_{sk}^{(nc)}\right) & \mathbf{0}_{2(M_y-1)d\times d^2} & \mathbf{0}_{2(M_z-1)d\times d^2} & \boldsymbol{\Upsilon}_{xk}^T \otimes \boldsymbol{K}_{x1}^{(nc)} - \boldsymbol{I}_d \otimes \boldsymbol{K}_{x2}^{(nc)} \\ \mathbf{0}_{2(M_x-1)d\times d^2} & \boldsymbol{I}_d \otimes \left(\boldsymbol{K}_{y1}^{(nc)} \tilde{\boldsymbol{U}}_{sk}^{(nc)}\right) & \mathbf{0}_{2(M_z-1)d\times d^2} & \boldsymbol{\Upsilon}_{yk}^T \otimes \boldsymbol{K}_{y1}^{(nc)} - \boldsymbol{I}_d \otimes \boldsymbol{K}_{y2}^{(nc)} \\ \mathbf{0}_{2(M_x-1)d\times d^2} & \mathbf{0}_{2(M_y-1)d\times d^2} & \boldsymbol{I}_d \otimes \left(\boldsymbol{K}_{z1}^{(nc)} \tilde{\boldsymbol{U}}_{sk}^{(nc)}\right) & \boldsymbol{\Upsilon}_{zk}^T \otimes \boldsymbol{K}_{z1}^{(nc)} - \boldsymbol{I}_d \otimes \boldsymbol{K}_{z2}^{(nc)} \\ \boldsymbol{\Upsilon}_{yk}^T \otimes \boldsymbol{I}_d - \boldsymbol{I}_d \otimes \boldsymbol{\Upsilon}_{yk} & \boldsymbol{I}_d \otimes \boldsymbol{\Upsilon}_{xk} - \boldsymbol{\Upsilon}_{xk} \otimes \boldsymbol{I}_d & \mathbf{0}_{d^2\times d^2} & \mathbf{0}_{d^2\times 2Md} \\ \mathbf{0}_{d^2\times d^2} & \boldsymbol{\Upsilon}_{zk}^T \otimes \boldsymbol{I}_d - \boldsymbol{I}_d \otimes \boldsymbol{\Upsilon}_{zk} & \boldsymbol{I}_d \otimes \boldsymbol{\Upsilon}_{yk} - \boldsymbol{\Upsilon}_{yk} \otimes \boldsymbol{I}_d & \mathbf{0}_{d^2\times 2Md} \\ \boldsymbol{I}_d \otimes \boldsymbol{\Upsilon}_{zk} - \boldsymbol{\Upsilon}_{zk} \otimes \boldsymbol{I}_d & \mathbf{0}_{d^2\times d^2} & \boldsymbol{\Upsilon}_{xk}^T \otimes \boldsymbol{I}_d - \boldsymbol{I}_d \otimes \boldsymbol{\Upsilon}_{xk} & \mathbf{0}_{d^2\times 2Md} \\ \mathbf{0}_{2Md\times d^2} & \mathbf{0}_{2Md\times d^2} & \mathbf{0}_{2Md\times d^2} & \tilde{\kappa}\boldsymbol{I}_{2Md} \end{bmatrix}. \tag{55}$$

Note that at each step of the iterative procedure, by reshaping the obtained vector, we can recover $\boldsymbol{\Upsilon}_{\xi k}$ and $\tilde{\boldsymbol{U}}_{sk}^{(nc)}$ as:

$$\tilde{\boldsymbol{U}}_{s(k+1)}^{(nc)} = \tilde{\boldsymbol{U}}_{sk}^{(nc)} + \Delta\hat{\boldsymbol{U}}_{s,k}^{(nc)} \tag{56}$$

and

$$\boldsymbol{\Upsilon}_{\xi(k+1)} = \boldsymbol{\Upsilon}_{\xi k} + \Delta\boldsymbol{\Upsilon}_{\xi k}, \quad \xi \in \{x, y, z\}. \tag{57}$$

The LS solution of (33) is chosen as the initial estimate of $\boldsymbol{\Upsilon}_\xi$. Meanwhile, the initial basis of the signal subspace is selected as $\tilde{\boldsymbol{U}}_{s0}^{(nc)} = \hat{\boldsymbol{U}}_s^{(nc)}$. The algorithm converges provided that $\min\{\|\Delta\boldsymbol{\Upsilon}_{\xi k}\|_F^2, \|\Delta\hat{\boldsymbol{U}}_{s,k}^{(nc)}\|_F^2\} \le \varepsilon$, $\xi \in \{x, y, z\}$, where $\xi$ is the tolerance.

REMARK This paper is only devoted to the derivation of the joint estimation approach for the spatial frequencies $\mu_{xi}$, $\mu_{yi}$, and $\mu_{zi}$, with $i = 1, \ldots, d$. However, the procedure explained above gives an arbitrary ordering of the solutions for the spatial frequencies $\mu_{xi}$, $\mu_{yi}$, and $\mu_{zi}$ on each axis. Association of $\mu_{\xi i}$, $\xi \in \{x, y, z\}$ to the same signal has been well studied in the literature. For example, an automatic pairing approach has been devised in [11] by forming a matrix, which is able to provide the same set of eigenvectors as $\boldsymbol{\Upsilon}_x$, $\boldsymbol{\Upsilon}_y$, and $\boldsymbol{\Upsilon}_z$ and unique eigenvalues for arbitrary arrival angles. As a result, the constructed matrix provides a unique ordering of the eigenvectors and eigenvalues for $\boldsymbol{\Upsilon}_x$, $\boldsymbol{\Upsilon}_y$, and $\boldsymbol{\Upsilon}_z$, and then the ordering of the spatial frequencies is uniquely determined. Moreover, an algorithm that achieves automatic pairing by simultaneously decomposing several nonsymmetric matrices is presented in [24]. Using (6) to (8), we can find that the signal parameters to be estimated, i.e., $\theta_i$ and $\phi_i$, $i = 1, \ldots, d$, are uniquely determined by the spatial frequencies $\mu_{xi}$, $\mu_{yi}$, and $\mu_{zi}$. As a result, we only evaluate the estimation accuracy of the spatial frequencies in Section IV.

## IV. SIMULATION RESULTS

In our simulations, we assume that there is a three-axis crossed array consisting of $M = 3m$ omnidirectional sensors, and each subarray has $m$ elements. The sensors are aligned along the $x$-, $y$-, and $z$-axes, as illustrated in Fig. 1. We evaluate the root mean square error (RMSE) according to the following definition:

$$\text{RMSE}_i = \sqrt{\frac{1}{M_c}\sum_{p=1}^{M_c}\sum_{\xi\in\{x,y,z\}}\left(\hat{\mu}_{\xi i}^{(p)} - \mu_{\xi i}\right)^2}, \tag{58}$$

where $M_c = 1000$ is the number of independent trials, and $\hat{\mu}_{\xi i}^{(p)}$, $\xi \in \{x, y, z\}$, $i = 1, \ldots, d$, are their estimated frequencies of the $i$th signal obtained in the $p$th trial, while $\mu_{\xi i}$, $\xi \in \{x, y, z\}$ are the corresponding true values. In all examples, we assume that there are two equipowered BPSK signals, and their initial phases are 5° and 20°. The number of array elements is set as $M = 30$, and all interelement spacings on the three subarrays are equal to $0.45\lambda_0$. For the improved SLS method, the tolerance is set to be $10^{-6}$. For comparison, the empirical results of the ESPRIT [3], SLS-ESPRIT [12], and NC-ESPRIT [18] are included. Moreover, in order to investigate the effect of the additional constraint on the SLS-ESPRIT and SLS-NC-ESPRIT algorithms, the empirical results of the SLS-ESPRIT and SLS-NC-ESPRIT methods without the additional constraint are provided as well.

### A. RMSE for $\theta_1 = \theta_2$, $\phi_1 \neq \phi_2$

When $\theta_1 = \theta_2$, it follows from (8) that $\mu_{z1} = \mu_{z2}$, namely, the two signals have same projection onto the $z$-axis. As a result, the equations in (32) for $\xi = z$ may be rank deficient, which will cause the ESPRIT, NC-ESPRIT, SLS-based schemes without the additional constraint to fail. Here, we assume the azimuths of the two BPSK signals are 0° and 20°, and their elevations are both 60°.

Fig. 2 compares the estimation accuracy of various approaches in terms of RMSE versus signal-to-noise ratio (SNR) in dB, where the number of snapshots is $N = 300$. It is indicated in Fig. 2 that the performances of the ESPRIT and the SLS-ESPRIT without the additional constraint deteriorate significantly even when the SNR is sufficiently large. Moreover, the ESPRIT and SLS-ESPRIT have a larger RMSE than the NC-based schemes because they do not make full use of the NC properties of the signals. For

the SLS-ESPRIT without the additional constraint, due to the rank deficiencies occurring in the SIEs associated with the $z$-axis of the array, it is inferior to the SLS-ESPRIT. Although the SLS-NC-ESPRIT without the additional constraint can provide more accurate DOA estimates, it still cannot resolve the two sources. However, from Fig. 2, we observe that the SLS-ESPRIT and SLS-NC-ESPRIT are still able to resolve the spatial frequencies, since they involve the additional constraint, which requires the SIEs of the three subarrays directed along the $x$-, $y$-, and $z$-axes to share the same set of eigenvectors. Moreover, as our proposal exploits the NC properties of the signals, it provides more accurate estimates than the SLS-ESPRIT.

In this example, we fix the number of snapshots at 20 and investigate the RMSE of the spatial frequency estimates as a function of SNR. It is observed in Fig. 3 that the proposed SLS-NC-ESPRIT still provides the smallest RMSE among all the approaches. The ESPRIT and SLS-ESPRIT without the additional constraint fail to provide accurate spatial frequency estimates because they cannot solve the rank-deficiency problem. Due to the fact that the NC-ESPRIT and SLS-NC-ESPRIT without the additional constraint make full use of the NC properties of the signals, they can provide smaller RMSE but still cannot resolve the two sources. Moreover, although the SLS-ESPRIT can handle the rank-deficiency problem, it is still slightly inferior to our proposed SLS-NC-ESPRIT.

The empirical results in Fig. 4 correspond to the scenario where the SNR is fixed at SNR $= -5$ dB while $N$ varies from 50 to 190. It is observed that the ESPRIT cannot handle the rank-deficiency problem and has a much larger RMSE than the other methods. Although the NC-ESPRIT can provide more accurate estimates than the ESPRIT, as it exploits the NC properties of the signals, it also suffers from the same problem as the ESPRIT. Furthermore, the SLS-based schemes without the additional constraint also have large errors due to the influence of rank deficiency. However, we observe that the rank-deficiency problem has little influence on the SLS-based schemes with the additional constraint. As the number of snapshots becomes larger, both the SLS-ESPRIT and SLS-NC-ESPRIT considerably improve in performance, but the former is still inferior to the latter.

### B. RMSE for $\theta_1 \neq \theta_2$, $\phi_1 \neq \phi_2$

In this example, we study the RMSE as a function of SNR. The number of snapshots is $N = 300$. Assume that the two BPSK signals arrive from $-4^\circ$ and $4^\circ$ in azimuth and from $18^\circ$ and $28^\circ$ in elevation. From Fig. 5, we observe that the proposed SLS-NC-ESPRIT provides the smallest RMSE among all the algorithms. Moreover, our proposed method significantly outperforms the other approaches in accuracy, especially when the SNR is less than $-5$ dB. Although there is no rank deficiency in this example, the SLS-ESPRIT and SLS-NC-ESPRIT still can provide better performance than the SLS-based schemes without the additional constraint because the former

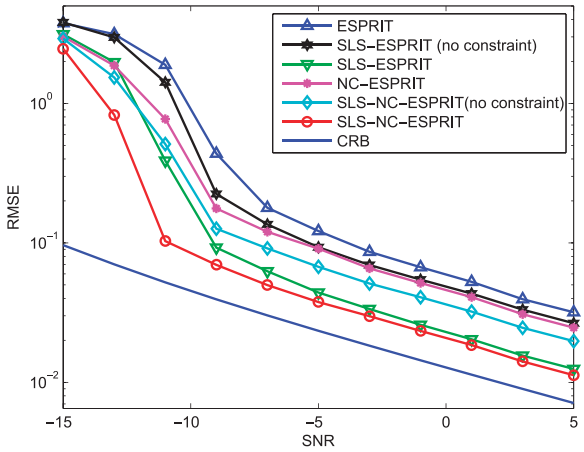


Fig. 5. RMSE of spatial frequency estimates versus SNR for $\theta_1 \neq \theta_2$, $\phi_1 \neq \phi_2$, $N = 300$.

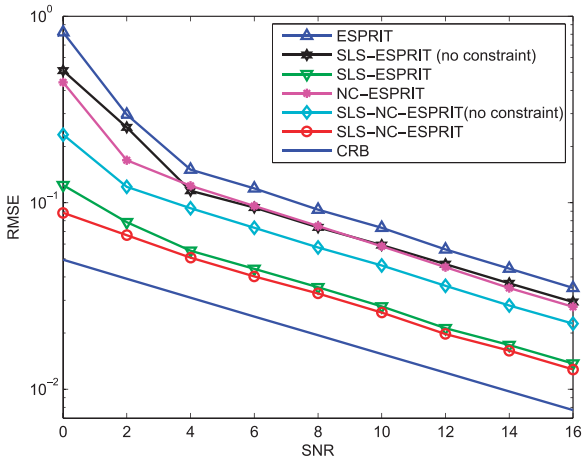


Fig. 6. RMSE of spatial frequency estimates versus SNR for $\theta_1 \neq \theta_2$, $\phi_1 \neq \phi_2$, $N = 20$.

exploit the fact that the matrices $\boldsymbol{\Upsilon}_\xi$, $\xi \in \{x, y, z\}$ share the same set of eigenvectors.

Fig. 6 shows the RMSEs of the investigated methods versus SNR at $N = 20$. All the algorithms can resolve the two sources because there is no rank deficiency. We can see that the proposed SLS-NC-ESPRIT still surpasses the other approaches even when the number of snapshots is small. The SLS-ESPRIT performs slightly worse than the SLS-NC-ESPRIT, because it does not exploit the NC properties of the signals. Furthermore, the SLS-NC-ESPRIT and SLS-ESPRIT can provide more accurate DOA estimates than the SLS-based schemes without the additional constraint. As no additional information is employed in the ESPRIT, it provides the largest RMSE among all the approaches.

The empirical results of these algorithms versus the number of snapshots for SNR $= -5$ dB are shown in Fig. 7. It is seen that the SLS-NC-ESPRIT and SLS-ESPRIT perform much better than the other methods. Since the proposed approach is able to utilize the NC properties of signals, it is superior to the SLS-ESPRIT in accuracy. Moreover, it is observed from Fig. 7 that the

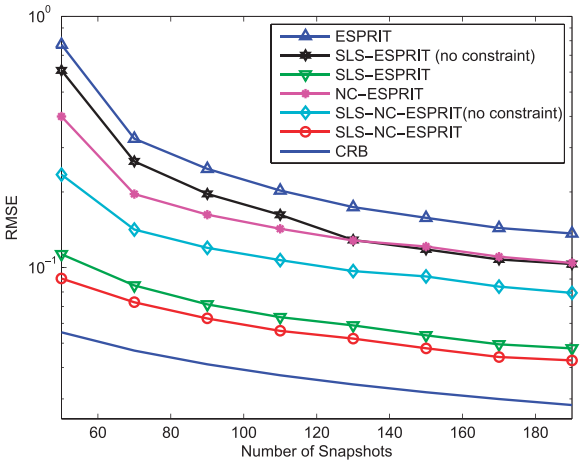


Fig. 7. RMSE of spatial frequency estimates versus snapshot number for $\theta_1 \neq \theta_2, \phi_1 \neq \phi_2$.

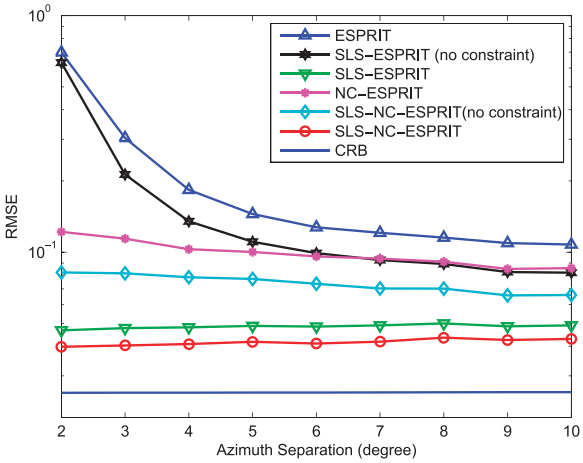


Fig. 8. RMSE of spatial frequency estimates versus azimuth separation.

NC-ESPRIT and SLS-NC-ESPRIT, which exploit the NC properties of the signals, achieve a performance improvement compared with their counterparts, i.e., ESPRIT and SLS-ESPRIT. As the additional constraint can guarantee much more accurate spatial frequency estimates, the SLS-ESPRIT and SLS-NC-ESPRIT provide smaller RMSE values than the SLS-based schemes without the additional constraint.

### C. RMSE versus Azimuth or Elevation Separation

We now examine the spatial frequency estimation errors as a function of azimuth separation, results of which are plotted in Fig. 8. The number of snapshots and SNR are 300 and $-5$ dB, respectively. We fix the DOAs of the first target at $(2^\circ, 18^\circ)$ and set the DOAs of the second target as $(2^\circ + \Delta\phi, 28^\circ)$, where $\Delta\phi$ varies from $2^\circ$ to $10^\circ$. It is indicated in Fig. 8 that our proposal outperforms the other algorithms. We can also see that the LS-based algorithms, that is, the ESPRIT and NC-ESPRIT, are considerably inferior to the proposed method. Moreover, the SLS-based schemes without the additional constraint can provide more accurate DOA estimates than the

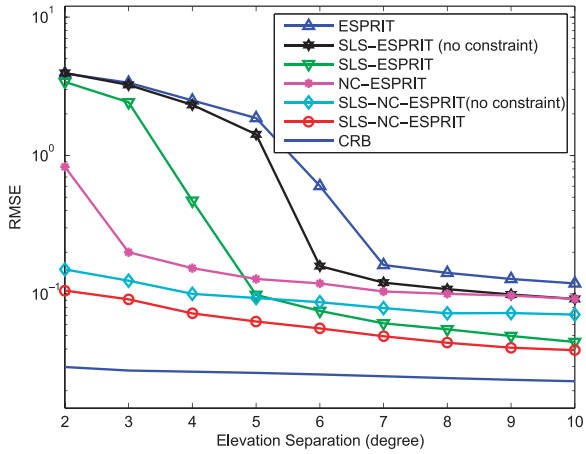


Fig. 9. RMSE of spatial frequency estimates versus elevation separation.

LS-based schemes. That is to say, the SLS-ESPRIT without the additional constraint is superior to the ESPRIT, and the SLS-NC-ESPRIT without the additional constraint outperforms the NC-ESPRIT. We can also observe that the SLS-ESPRIT and SLS-NC-ESPRIT, which exploit the fact that the matrices $\boldsymbol{\Upsilon}_\xi, \xi \in \{x, y, z\}$ share the same set of eigenvectors, have much smaller RMSE values than the SLS-based schemes without the additional constraint. Furthermore, the performance of the proposed SLS-NC-ESPRIT is not sensitive to the azimuth separation. It is well known that the DOA estimation algorithm will obtain much more accurate estimates when $\sum_{\xi\in\{x,y,z\}} |\mu_{\xi 1} - \mu_{\xi 2}|$ becomes larger. From (6) and (7), we can conclude that both the spatial frequencies projected on the $x$- and $y$-axes are affected by the azimuth $\phi$. In this example, when $\Delta\phi$ increases from $2^\circ$ to $10^\circ$, according to (6) to (8), $|\mu_{x1} - \mu_{x2}|$ is an increasing function, while $|\mu_{y1} - \mu_{y2}|$ is a decreasing function. Consequently, $\sum_{\xi\in\{x,y,z\}} |\mu_{\xi 1} - \mu_{\xi 2}|$increases a little bit, and the azimuth separation may have little influence on the RMSE of the proposed approach. Moreover, as a SLS-based scheme, the SLS-ESPRIT has a significant performance improvement compared with the ESPRIT, and it is also independent of azimuth separation. Nevertheless, it is still inferior to the proposed solution.

Fig. 9 shows the spatial frequency estimate errors as a function of elevation separation. The number of snapshots and SNR are set as 300 and $-5$ dB, respectively. We fix the DOAs of the first target at $(-4^\circ, 18^\circ)$ and set the DOAs of the second target as $(4^\circ, 18^\circ + \Delta\theta)$. Here, $\Delta\theta$ increases from $2^\circ$ to $10^\circ$. It is indicated that when the separation of elevation angles is less than $5^\circ$, the proposed SLS-NC-ESPRIT yields a significant performance improvement over the other methods. As the ESPRIT and NC-ESPRIT ignore the overlapping subarray configurations, they can only provide inferior estimation accuracy. Moreover, the SLS-based schemes are superior to the LS-based schemes, that is, the ESPRIT and

NC-ESPRIT. However, the SLS-ESPRIT and SLS-NC-ESPRIT outperform the SLS-based schemes without the additional constraint because the former fully exploit the relationship of the matrices $\boldsymbol{\Upsilon}_{\xi}, \xi \in \{x, y, z\}$. Although the SLS-ESPRIT is able to efficiently utilize the overlapping structure between the subarrays, it does not employ the NC properties of the signals. This is why it is inferior to the proposed method, especially for $\Delta\theta < 5^{\circ}$.

## V. CONCLUSION

An improved SLS-NC-ESPRIT method has been developed for accurate DOA estimation of NC signals with a three-axis crossed array. The proposed scheme exploits the NC properties of the signals and accounts for the errors in the signal subspace by using an iterative minimization procedure to optimize the signal subspace estimate. In order to circumvent the rank-deficiency problem, an additional constraint has been used in solving the invariance equations of the three linear subarrays directed along the $x$-, $y$-, and $z$-axes. Consequently, the devised method is able to provide considerable improvement in estimation accuracy. It is shown that the proposed method is superior to the state-of-the-art algorithms in terms of estimation performance, especially at low SNR conditions.

## REFERENCES


[1] Li, F., and Vaccaro, R. J.
Analysis of min-norm and MUSIC with arbitrary array geometry,
*IEEE Transactions on Aerospace and Electronic Systems*, **26**, 6 (1990), 976–985.

[2] Rao, B. D., and Hari, K. V. S.
Performance analysis of root-MUSIC.
*IEEE Transactions on Acoustics, Speech, and Signal Processing*, **37**, 12 (1989), 1939–1949.

[3] Roy, R., and Kailath, T.
ESPRIT-estimation of signal parameters via rotational invariance techniques.
*IEEE Transactions on Acoustics, Speech, and Signal Processing*, **37**, 7 (1989), 984–995.

[4] Roy, R., Paulraj, A., and Kailath, T.
ESPRIT—A subspace rotation approach to estimation of parameters of cisoids in noise.
*IEEE Transactions on Acoustics, Speech, and Signal Processing*, **34**, 5 (1986), 1340–1342.

[5] Rosen, J. B., Park, H., and Glick, J.
Total least norm formulation and solution for structured problems.
*SIAM Journal on Matrix Analysis and Applications*, **17**, 1 (1996), 110–126.

[6] Li, F., and Vaccaro, R. J.
Sensitivity analysis of DOA estimation algorithms to sensor errors.
*IEEE Transactions on Aerospace and Electronic Systems*, **28**, 3 (1992), 708–717.

[7] Haardt, M.
Structured least squares to improve the performance of ESPRIT-type algorithms.
*IEEE Transactions on Signal Processing*, **45**, 3 (1997), 792–799.

[8] Li, F., Liu, H., and Vaccaro, R. J.
Performance analysis for DOA estimation algorithms: Unification, simplification, and observations.
*IEEE Transactions on Aerospace and Electronic Systems*, **29**, 4 (1993), 1170–1184.

[9] Mathews, C. P., and Zoltowski, M. D.
Eigenstructure techniques for 2-D angle estimation with uniform circular arrays.
*IEEE Transactions on Signal Processing*, **42**, 9 (1994), 2395–2407.

[10] Zoltowski, M. D., Haardt, M., and Mathews, C. P.
Closed-form 2-D angle estimation with rectangular arrays in element space or beamspace via unitary ESPRIT.
*IEEE Transactions on Signal Processing*, **44**, 2 (1996), 316–328.

[11] Eckhoff, R.
Direction-of-arrival determination using 3-axis crossed array and ESPRIT.
In *Proceedings of the IEEE International Symposium on Indoor and Mobile Radio Communications*, Boston, MA, Sep. 1998, 471–475.

[12] Kwakkernaat, M., Jong, Y., and Bultitude, R.
Improved structured least squares for the application of unitary ESPRIT to cross arrays.
*IEEE Signal Processing Letters*, **13**, 6 (2006), 349–352.

[13] Kwakkernaat, M., Jong, Y., Bultitude, R., and Herben, M.
High-resolution angle-of-arrival measurements on physically-nonstationary mobile radio channels.
*IEEE Transactions on Antennas and Propagation*, **56**, 8 (2008), 2720–2729.

[14] Abeida, H., and Delmas, J. P.
MUSIC-like estimation of direction of arrival for noncircular sources.
*IEEE Transactions on Signal Processing*, **54**, 7 (Jul. 2006), 2678–2690.

[15] Charge, P., Wang, Y., and Saillard, J.
A non-circular sources direction finding method using polyomial rooting.
*Signal Processing*, **81**, 8 (Aug. 2001), 1765–1770.

[16] Zoubir, A., Charge, P., and Wang, Y.
Non circular sources localization with ESPRIT.
In *Proceedings of the European Conference on Wireless Technology (ECWT 2003)*, Munich, Germany, Oct. 2003.

[17] Haardt, M., and Romer, F.
Enhancements of unitary ESPRIT for non-circular sources.
In *Proceedings of the IEEE International Conference on Acoustics, Speech, and Signal Processing (ICASSP)*, Montreal, Canada, May 2004, 101–104.

[18] Steinwandt, J., Romer, F., and Haardt, M.
Performance analysis of ESPRIT-type algorithms for non-circular sources.
In *Proceedings of the IEEE International Conference on Acoustics, Speech, and Signal Processing (ICASSP)*, Vancouver, Canada, May 2013, 3986–3990.

[19] Steinwandt, J., Romer, F., Haardt, M., and Del Galdo, G.
R-dimensional ESPRIT-type algorithms for strictly second-order non-circular sources and their performance analysis.
*IEEE Transactions on Signal Processing*, **62**, 18 (Sep. 2014), 4824–4838.

[20] Wax, M., and Ziskind, I.
Detection of the number of coherent signals by the MDL principle.
*IEEE Transactions on Acoustics, Speech, and Signal Processing*, **37**, 8 (Aug. 1989), 1190–1196.

[21] Wax, M., and Kailath, T.
Detection of signals by information theoretic criteria.
*IEEE Transactions on Acoustics, Speech, and Signal Processing*, **33**, 2 (Apr. 1985), 387–392.

[22] Huang, L., Wu, S., and Li, X.
Reduced-rank MDL method for source enumeration in high-resolution array processing.
*IEEE Transactions on Signal Processing*, **55**, 12 (Dec. 2007), 5658–5667.

[23] Huang, L., Long, T., Mao, E., and So, H. C.
MMSE-based MDL method for robust estimation of number of sources without eigendecomposition.
*IEEE Transactions on Signal Processing*, **57**, 10 (Oct. 2009), 4135–4142.

[24] Haardt, M., and Nossek, J. A.
Simultaneous Schur decomposition of several nonsymmetric matrices to achieve automatic pairing in multidimensional harmonic retrieval problems.
*IEEE Transactions on Signal Processing*, **46**, 1 (Oct. 1998), 161–169.

**Yunmei Shi** was born in Shandong, China. She received the B.Sc. degree in electronic and information engineering from Harbin Institute of Technology at Weihai, Weihai, China, in 2012, and the M.Sc. degree in electronic and communication engineering from Harbin Institute of Technology Shenzhen Graduate School, Shenzhen, China, where she is currently pursuing the Ph.D. degree, in 2014.

Her research interests include sensor array processing, statistical signal processing, convex optimization, and sparse signal representation.

**Lei Huang** (M'07—SM'14) was born in Guangdong, China. He received the B.Sc., M.Sc., and Ph.D. degrees in electronic engineering from Xidian University, Xian, China, in 2000, 2003, and 2005, respectively.

From 2005 to 2006, he was a research associate with the Department of Electrical and Computer Engineering, Duke University, Durham, NC. From 2009 to 2010, he was a research fellow with the Department of Electronic Engineering, City University of Hong Kong, and a research associate with the Department of Electronic Engineering, The Chinese University of Hong Kong. From 2012 to 2014, he was a full professor with the Department of Electronic and Information Engineering, Harbin Institute of Technology Shenzhen Graduate School. Since November 2014, he has joined the College of Information Engineering, Shenzhen University, where he is currently a chair professor. His research interests include spectral estimation, array signal processing, statistical signal processing, and their applications in radar and wireless communication systems.

He is currently an associate editor of *IEEE Transactions on Signal Processing* and an editorial board member of *Digital Signal Processing*.

**Cheng Qian** was born in Zhejiang on November 27, 1988. He received the B.E. degree in communication engineering from Hangzhou Dianzi University, Hangzhou, China, in 2011, and the M.E. degree in information and communication engineering from Harbin Institute of Technology (HIT), Shenzhen, China, in 2013. He is currently pursuing the Ph.D. degree in the field of information and communication engineering at HIT. His research interests are in array signal processing and *multiple-input–multiple-output* (MIMO) radar.

**Hing Cheung So** (S'90–M'95–SM'07–F'15) was born in Hong Kong. He received the B.Eng. degree from the City University of Hong Kong and the Ph.D. degree from The Chinese University of Hong Kong, both in electronic engineering, in 1990 and 1995, respectively. From 1990 to 1991, he was an electronic engineer with the Research and Development Division, Everex Systems Engineering Ltd., Hong Kong. During 1995–1996, he was a postdoctoral fellow with The Chinese University of Hong Kong. From 1996 to 1999, he was a research assistant professor with the Department of Electronic Engineering, City University of Hong Kong, where he is currently an associate professor. His research interests include statistical signal processing, fast and adaptive algorithms, signal detection, robust estimation, source localization and sparse approximation.

Dr. So has been on the editorial boards of *IEEE Signal Processing Magazine* (2014–), *IEEE Transactions on Signal Processing* (2010–2014), *Signal Processing* (2010–), and *Digital Signal Processing* (2011–). In addition, he is an elected member in Signal Processing Theory and Methods Technical Committee (2011–) of the IEEE Signal Processing Society where he is chair in the awards subcommittee (2015–). He has been elected Fellow of IEEE in recognition of his contributions to spectral analysis and source localization in 2015